https://doi.org/10.5194/egusphere-2026-3037
Preprint. Discussion started: 18 June 2026

Insights into stress-loading mechanisms in the western Peloponnese, Greece from a high-resolution earthquake catalog

David Essing[1], Gian Maria Bocchini[1], Marco Pascal Roth[1], Anna Serpetsidaki[2], Ioanna Nikolopoulou[2], Rebecca Maria Harrington[1], Efthimios Sokos[2]

[1]Institute of Geosciences, Ruhr-University Bochum, Bochum, 44780, Germany
[2]Seismological Laboratory, Geology Department, University of Patras, GR-26504 Patras, Greece

Correspondence to: David Essing (david.essing@rub.de)

Abstract. The western Peloponnese exhibits a continuum of earthquake faulting styles that reside in a complex stress field near the western termination of the Hellenic Subduction System. Here we present a detailed study of recent seismicity in western Peloponnese, including the spatiotemporal distribution of earthquake sequences and their clustering and migration properties to infer possible driving mechanisms. We build a detailed earthquake catalog from December 2023 – September 2024 with a magnitude-of-completeness M_c ~1 and a location precision on the order of 100 s of meters by combining new data from temporary seismic station deployments with publicly available data from permanent stations. Catalog statistical and clustering analysis shows increased background seismicity rates and seismic moment release in the northern part of the study area that is consistent with larger strain rates and a higher stressing rate reported from geodetic data. The seismicity distribution and focal mechanism solutions suggest that the predominantly north-south extensional regime in the north changes to east-west extension in the central-western Peloponnese near the town of Zaharo. Nearest-neighbor cluster analysis reveals mainshock-aftershock-type sequences in the northwest near the town of Vartholomio that are consistent with tectonic loading. Conversely, clustering properties in the central-western Peloponnese near Zaharo are consistent with swarm-like sequences driven by external forcing, such as pore-fluid pressure changes, and potential aseismic slip. Independent studies of slab dewatering suggest fluid-driven pore-pressure gradients that might be responsible for migrating seismicity and swarm-like behavior in the upper plate.

1 Introduction

Peloponnese lies along the Western margin of the Hellenic Subduction System, Greece, where the Nubian slab is currently subducting beneath the Aegean plate at a rate of 30-35 mm yr^{-1} (McClusky et al., 2000; Reilinger et al., 2006). Peloponnese and the offshore region to the west host a complex tectonic setting, as evidenced by the variety of faulting styles present over regional length scales (Fig. 1). For example, the Corinth rift to the north is opening at 10–15 mm yr^{-1} in a N-S direction (Briole et al., 2000; Avallone et al., 2004) and hosts predominantly normal-style faulting (Pacchiani & Lyon-Caen, 2010). Normal style faulting also occurs in the southern Peloponnese, and has hosted notable M > 5 earthquakes in 1986 and 2004

https://doi.org/10.5194/egusphere-2026-3037
Preprint. Discussion started: 18 June 2026

near the city of Kalamata (Kassaras et al., 2014), and possibly near Sparta in 464 BCE (Armijo et al., 1991). The northwestern border of Peloponnese hosts the Kefalonia Transform fault system that marks the transition between oceanic subduction to the south and continental collision to the north (Louvari et al., 1999) and accommodates right-lateral, strike-slip deformation. The Movri fault is located further inland to the east, and it also exhibits right-lateral slip that is roughly parallel to the Kefalonia Transform fault (Feng et al., 2010). The Movri fault is proposed to represent the southern edge of the Ionian-Akarnania Block, as suggested by geological (Pérouse et al., 2017) and geodetic (Chousianitis et al., 2015) approaches, with limited studies of its seismicity, to date (Haddad et al., 2020). Active subduction mostly dominated by reverse faulting occurs to the west and southwest of the study area (Kiratzi & Louvari, 2003), which means that all end-member faulting styles are present in western Greece. In this study, we focus on the northwestern Peloponnese that extends roughly from the Gulf of Corinth in the north to Kalamata in the south (Fig. 1). The region has hosted notable, felt earthquakes in the recent years, such as the M_w 6.4 Movri sequence in 2008 (Gallovič et al. 2009; Papadopoulos et al. 2010) and the M_w 5.5 Vartholomio earthquake in 2002 (Serpetsidaki et al., 2010).

The complex tectonic setting is also evident from GNSS observations (Chousianitis et al., 2015; D'Agostino et al., 2020; Lazos et al., 2025), that document a regional transition from a compressional to an extensional strain regime from west to east from the southwestern Balkans to the Peloponnese. For example, D'Agostino et al. (2020) interprets the boundary between the two regimes to roughly coincide with the western coastline of the Peloponnese Peninsula. D'Agostino et al. (2020) also observe a change in the extensional direction from north-south near the Corinth rift to east-west near the center of the Peloponnese, which is consistent with other geodetic studies (Chousianitis et al., 2015; Lazos et al., 2025). The change in extensional direction is also interpreted from focal mechanism solutions and stress inversion results (Konstantinou et al., 2017). While various studies interpret a change in the stress regime from north to south, they differ in the spatial resolution. For instance, Chousianitis et al. (2015), D'Agostino et al. (2020), and Konstantinou et al. (2017) employed continuous grid-based strain modeling to analyze crustal deformation across the Peloponnese and find a gradual spatial transition in the direction of crustal strain from the northern to the central part of the peninsula. In contrast, a recent study by Lazos et al. (2025) reveals more complex deformation that is marked by generally low strain rates punctuated by localized zones of elevated strain, which they interpret to result from heterogeneous loading. While the spatial scale of stress heterogeneity may be under debate, the general consensus is that the heterogeneous observed strain rates imply that the stress field is also heterogeneous. Part of the discrepancy in interpretation is due to the resolution of geodetic observations.

Another key question is how the heterogeneous stress is being released through seismic and aseismic deformation? Is deformation localized primarily as discrete slip that occurs on well-defined fault planes, or does it occur through distributed micro-seismicity across a broader, diffuse crustal volume? While stress is difficult to measure directly in the Earth's crust, we can infer loading properties and kinematic relationships of active faults by studying seismic deformation through detailed catalogs. We can also tease out clues of aseismic deformation indirectly through statistical, clustering, and migration properties of small earthquakes in detailed catalogs.

https://doi.org/10.5194/egusphere-2026-3037
Preprint. Discussion started: 18 June 2026

Here we present a new, high-resolution earthquake catalog, spanning from 01 December 2023 until 30 September 2024, built using data from both permanent and newly deployed temporary stations to study the statistical and clustering properties of earthquake sequences in the western Peloponnese. In addition to the catalog, we calculate moment tensor solutions for five, onshore earthquakes ($M > 3$) to provide further observational constraints on the regional stress field. In the following, we will present the features of the new catalog and results of nearest-neighbor clustering analysis. We will show that the background seismicity during the observational period supports geodetic observations of a gradual decrease in tectonic loading rates from north to south. In addition, clustering properties of two notable sequences suggest different loading mechanisms are at work in the region, namely tectonically driven earthquakes vs. sequences driven by external forcing mechanisms, such as fluid movement that may originate from slab dewatering. We start with a methodological description of catalog building, focal mechanism determination, and nearest-neighbor clustering analysis. We follow with a presentation of the results, and discussion of their implication for loading. We conclude by summarizing the implications of this work that relate the detailed picture of seismicity generated here to geodetic observations and relate them to plausible loading conditions.

https://doi.org/10.5194/egusphere-2026-3037
Preprint. Discussion started: 18 June 2026

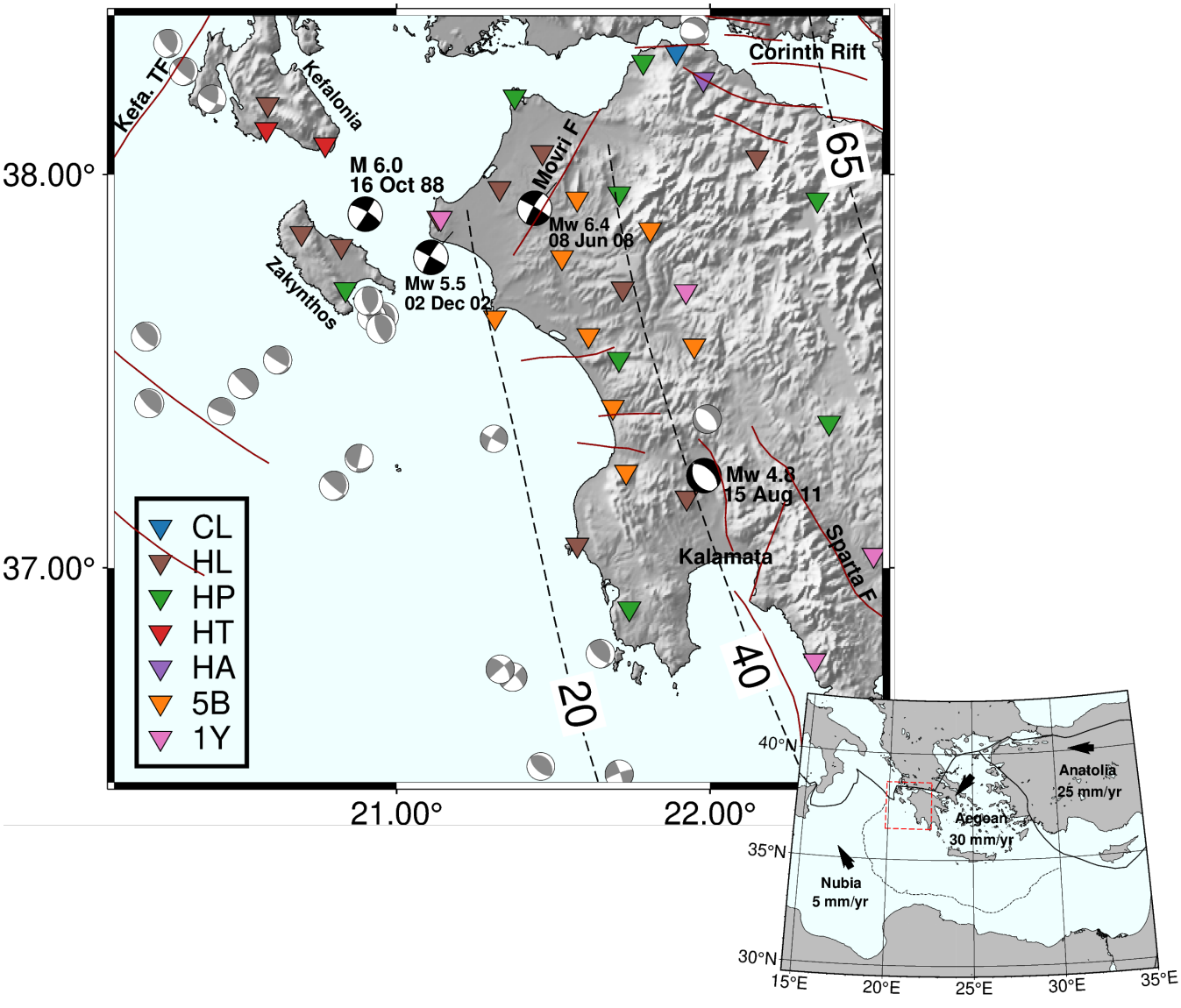

Figure 1: Study area with new and long-term seismic station data used for this work, color-coded by network (CL: Corinth Rift Laboratory, HL: National Observatory of Athens; HP: University of Patras; HT: Aristotle University of Thessaloniki; HA: University of Athens; 5B: RUB Observational Geophysics Lab; 1Y: AdriaArray Temporary Network; Greece, North Macedonia). Grey focal mechanisms for earthquakes (M > 5.5) are from the European-Mediterranean Regional Centroid-Moment Tensors Catalog (Pondrelli, 2002). Black focal mechanisms for larger earthquakes are discussed in the text (Ganas et al., 2009; Kassaras et al., 2014; Papazachos et al., 1998; Serpetsidaki et al., 2014). Dashed black lines indicate top-of-slab isodepth lines from Bocchini et al. (2018). Brown lines indicate upper-crustal faults (DISS Working Group, 2021). Inset: Study area within the eastern Mediterranean Sea. Black lines indicate boundaries between major tectonic plates (modified from Bird, 2003). GPS-velocities relative to a fixed Eurasian plate (Reilinger et al., 2006).

https://doi.org/10.5194/egusphere-2026-3037
Preprint. Discussion started: 18 June 2026

2 Catalog Building

The following section details the catalog-building procedure that uses the combined network of permanent and temporary stations for the period 01 December 2023 - 30 September 2024. Section 2.1 presents the network configuration, and the detection and location processing steps follow in Sections 2.2-2.3. Section 2.4 outlines magnitude estimation and is followed by the description of focal mechanism inversion in Section 2.5.

2.1 Seismic Network

The seismic network used for catalog building consists of 33 broadband seismic stations across the western Peloponnese aimed at lowering the magnitude of completeness (M_c) and improving hypocentral location quality relative to routine monitoring practice. The densified array combines one Corinth Rift Laboratory station (Corinth Rift Laboratory Team And RESIF Datacenter, 2013), four Adria Array stations (Friederich et al., 2022), 20 Hellenic Unified Seismic Network stations (National Observatory of Athens, 1975; Aristotle University of Thessaloniki, 1981; University of Patras, 2000; University of Athens, 2008), and eight broadband seismic stations from a temporary deployment operated by the Observational Geophysics Laboratory of the Ruhr-University Bochum (RUB) (Harrington et al., 2023) that began in December 2023 (Fig. 1). The eight additional RUB stations (Harrington et al., 2023) reduce the average interstation distance from 50.1 km to 46.9 km and increase coverage in the northwestern Peloponnese (Fig. 1; Fig. 2; Fig. S2).

2.2 Earthquake Detection

We begin by automatically detecting seismic phase arrivals using PhaseNet (Zhu & Beroza, 2019) trained on the INSTANCE dataset (Michelini et al., 2021), applied to raw, continuous three-component waveforms sampled at 100 Hz (200 Hz for the 5B RUB-network stations). Because we consider seismicity from the overriding continental plate, the Hellenic slab, and the interface between them, the INSTANCE dataset is well suited for the study area, because it consists of both crustal seismicity and events from the Calabrian subduction zone. We scan continuous waveforms for the entire 10-month data set from all 33 stations to detect P & S-phase arrivals and retain picks with a probability greater than 0.1 (Fig. S1). The automated phase picking step enables us to scan the ~400 GB set of waveforms in an automated workflow while optimizing computational time.

Next, we associate potential phase picks at neighboring stations using the PyOcto package (Münchmeyer, 2023) for cases where move-out is consistent with typical velocity values of the underlying general 1D velocity model (Hatzfeld et al., 1990). We use the P-wave velocity model from Hatzfeld et al. (1990) and a Vp-Vs-ratio of 1.81 that is derived from events in our catalog and is consistent with previous work in the study area (e.g., Kassaras et al., 2016; Sachpazi et al., 2020). We classify sets of associated picks as new events for cases with at least eight phase picks on a minimum of three stations with both P and S picks. We avoid cases with small interevent times that may lead to erroneous phase associations by requiring a

https://doi.org/10.5194/egusphere-2026-3037
Preprint. Discussion started: 18 June 2026

minimum interevent time of 10 seconds. In cases of multiple earthquakes occurring within a 10 seconds window, we retain the event with the largest number of picks.

2.3 Earthquake Location

We estimate initial absolute earthquake locations using the NLLoc algorithm (Lomax et al., 2000). NLLoc addresses the full non-linear inverse problem and demonstrates an improved robustness to outliers. It provides reliable location and error estimates, even in challenging cases with poor azimuthal coverage and a strongly heterogeneous velocity model. We adopt a detailed 1D velocity model that combines the two shallowest layers from Kassaras et al. (2014) with deeper layers from Sachpazi et al. (2020) and uses a constant Vp-Vs-ratio of 1.81 as derived from the data (Tab. S1). We refine the initial locations by applying the multi-scale, high-precision NLL-SSST-coherence method (Lomax & Savvaidis, 2022). The method combines source-specific station travel-time corrections (SSSTs) that account for possible 3D velocity heterogeneity with probabilistic stacking of location PDFs based on interevent waveform coherence. The SSST corrections result from using iterative spatial smoothing with decreasing kernel size down to a minimum smoothing distance that is determined by the degree of spatial organization of seismicity (Lomax & Savvaidis, 2022). We test a range of smoothing distances and find through a data-driven approach that a minimum of 4 km is the most suitable for our station-seismicity distribution. The SSST calculation uses high-quality hypocentral locations with root mean square (RMS) error ≤ 0.35 s, phase arrivals ≥ 16, azimuthal gap ≤ 240°, and a maximum semi-major axis of the location uncertainty ellipse ≤ 5 km that sample the area of interest. The resulting SSSTs are spatially heterogeneous and phase- and station-specific, allowing location-dependent travel-time adjustments across the 3D volume.

Based on the assumption that events that exhibit highly similar waveforms are nearly co-located (Gao et al., 2021; Geller & Mueller, 1980), we quantify their waveform coherence to improve relative earthquake locations. We then use the resulting coherence values as weights for stacking the location PDFs derived from the SSST relocations, which significantly reduces aleatoric uncertainties and enhances the relative location of clustered events (Lomax & Savvaidis, 2022). We compute waveform coherence using a 2 – 6 Hz bandpass filter at 10 seismic stations (Fig. 2). The 6 Hz upper cutoff is consistent with the ¼-wavelength criterion, and it corresponds to a theoretical location precision of ~ 250 m, assuming a mean P-wave velocity of 5.8 km s^{-1}.

2.4 Magnitude Estimation

We estimate local magnitudes (M_L) following Hutton & Boore (1987) using a parameterization that accounts for geometrical spreading through the factor n, as well as the anelastic attenuation coefficient, K, appropriate for the study area (Scordilis et al., 2016). We convert waveforms to displacement on a Wood-Anderson seismometer (Uhrhammer & Collins, 1990) and compute the local magnitude using the following:

$$M_L = \log_{10}(A) + n * \log_{10}(R/100) + K * (R - 100) + 3.0 \quad (1),$$

https://doi.org/10.5194/egusphere-2026-3037
Preprint. Discussion started: 18 June 2026

where n = 1.319, K = 0.00226, where A is the 0-to-peak S-Wave amplitude in nm and R the hypocentral distance in km. We first estimate M_L separately for each horizontal component, then compute a station-level average from the two components. The final magnitude estimate then results from a network-wide estimate across all stations, with a minimum requirement of three stations (Fig. S1). We subsequently estimate the catalog completeness magnitude, M_c, using the Maximum Curvature method and add an offset of 0.2 to the reported M_c, to account for potential M_c underestimation (Wiemer & Wyss 2000; Woessner & Wiemer 2005). We estimate the b-value using the b-positive method (van der Elst, 2021).

Both local and moment magnitudes can exhibit systematic differences for earthquakes with M < 3 (Hanks & Boore, 1984; Baltay & Abercrombie, 2025). We therefore additionally estimate the seismic moment M_0 for all events using spectral fitting. We limit our approach to S-waves and use magnitude-dependent time windows that are refined based on event-station distances following Bindi et al. (2020). We estimate event spectra using a multi-taper approach (Prieto, 2022) for stations with a signal to noise ratio (SNR) > 3 in the frequency band of peak energy (see Supplement Information Text 1). We fit the S-wave spectra using a Boatwright (1980) model and use the resulting long-period spectral amplitude Ω_0 and distance to obtain the seismic moment M_0 (Brune, 1970), and then compute the M_w value (e.g., Abercrombie, 1995; Kanamori & Brodsky, 2004). We report M_w for events with > 6 M_0 estimates.

2.5 Moment Tensor (MT) Estimation

We perform MT inversion for the five, well constrained events that occurred within the upper 15 km of the overriding plate (3.5 < M_w < 4.8), using the ISOLA algorithm (Sokos & Zahradník, 2008; Zahradník, & Sokos, 2018) and broadband waveforms from both temporary and permanent stations. ISOLA uses complete waveforms and computes full-waveform Green's functions using the discrete-wavenumber method. We perform MT inversion in the frequency band of 0.11-0.16 Hz because it provides optimal variance reduction. The lower and upper frequency limits are defined by the SNR and the instrument frequency response, and by the crustal model accuracy, respectively. We adopt the same 1D velocity model used in the event location (Tab. S1) for the Green's function calculation to ensure consistency.

The MT results are expressed in terms of the double-couple component of the deviatoric solution represented by the scalar moment, strike, dip, and rake. To evaluate the reliability of each solution, we systematically cross-check the predicted and observed P-wave first-motion polarities at each station (Fig. S3).

A common quantitative measure of MT solution quality is variance reduction, a measure of the overall misfit between observed and synthetic (modeled) waveforms. Because the variance reduction does not always provide a reliable measure of solution quality (Sokos & Zahradník, 2008), we also consider the following quality measures to quantify the stability of the solution: the number of stations, and the condition number (CN), which quantifies the solution stability based on linear inversion theory, the Focal-Mechanism VARiability Index (FMVAR) and the Space-Time VARiability Indexes (STVAR) (Sokos & Zahradník, 2013), both of which quantify the variability of the solution in the vicinity of the best-fitting source. Since the MT inversion is performed over a grid of possible source locations and time steps, STVAR is particularly suited to assess the solution variability in space and time, while FMAVR is related to MT variability around the best-fitting source.

https://doi.org/10.5194/egusphere-2026-3037
Preprint. Discussion started: 18 June 2026

The most favorable solutions are those for which both FMVAR and STVAR indexes are small (Sokos & Zahradník, 2013). The quantification of the focal mechanism variability in FMVAR is done via the Kagan angle (Kagan, 1991). This method considers the statistical analysis of double-couple earthquake focal mechanism orientation and calculates the minimum rotation angle between two focal mechanisms. The angle can vary from 0° (perfect agreement between two solutions) to 120° (total disagreement), where values below 60° are commonly used as a threshold for good agreement (Pondrelli et al., 2006). We refer the reader to Table S2 for numerical data related to the MT solutions, including numerical quality-control metrics.

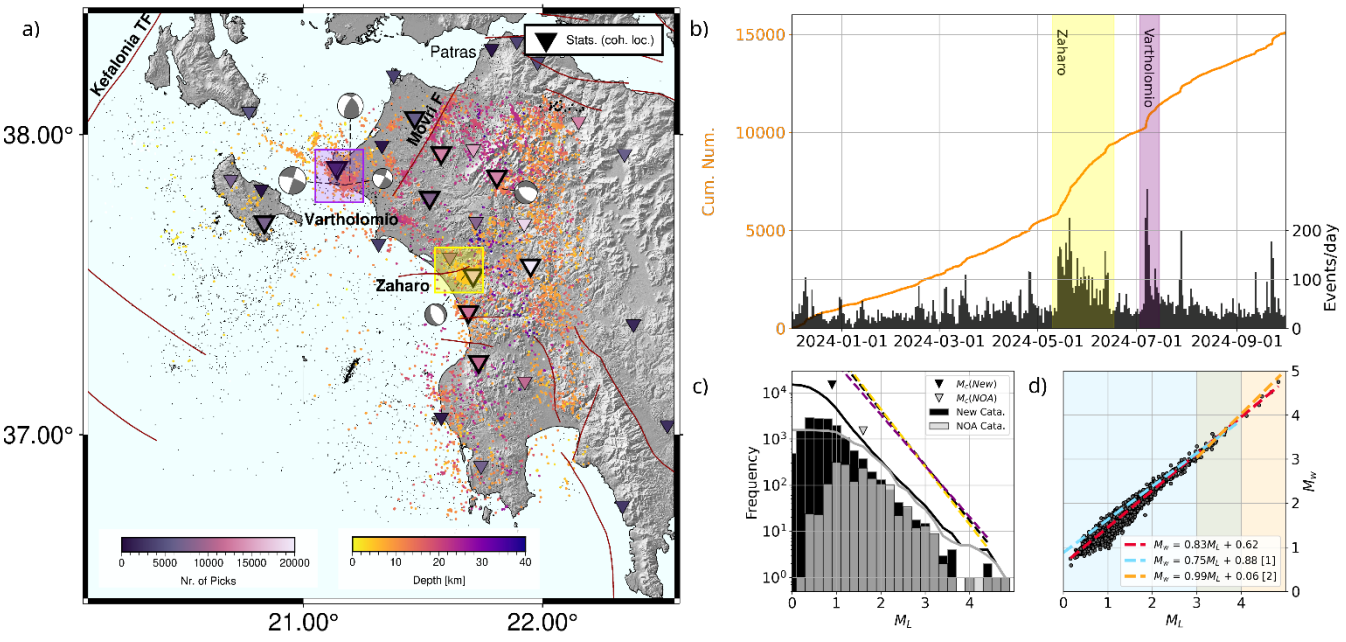

Figure 2: (a) Study area map with the densified array color-coded by the number of picks they contributed to the earthquake catalog. Stations used for waveform coherence-based locations (coh. loc.) are outlined by a thick black line. New earthquake detections used in this study are color-coded according to the depth. Black dots indicate newly detected seismicity from 1 km above the slab interface to greater depths that are not analyzed. Focal mechanism estimates of the five largest crustal events that occurred during the study period (3.4 < M_w < 4.8) shown in gray and mapped crustal faults in dark red (DISS Working Group, 2021). (b) Histogram of seismicity in 24-hour bins, with cumulative number shown by the orange curve (see text). (c) Frequency-Magnitude distribution based on estimated local magnitude (M_L) for newly detected earthquakes (black) and NOA cataloged events (gray). Triangles indicate magnitude of completeness for this study (M_c = 0.9) and the NOA catalog (M_c = 1.6). Dashed lines indicate b-values for the catalog (black, b = 1.19±0.02), the Zaharo sequence (yellow, b = 1.25±0.06), and the Vartholomio sequence (purple, b = 1.1±0.07). (d) Moment magnitudes (M_w) vs. M_L for this study. Red dashed line indicates the fit for this study, blue dashed line and shaded area are the fit and magnitude range found in [1] Ross et al. (2016), and orange dashed line and shaded area are the fit and magnitude range found in [2] Konstantinou & Melis (2018) (see text).

3 Nearest-Neighbor Clustering

How earthquakes cluster in space and in time is strongly related to the triggering mechanism (e.g., Ben-Zion, 2008; Freed, 2005; Utsu & Ogata, 1995; Utsu, 2002). For example, earthquake foreshocks and aftershocks concentrate over varying spatial scales and with different typical interevent times (Felzer et al., 2004; Helmstetter et al., 2005; Kisslinger & Jones,

https://doi.org/10.5194/egusphere-2026-3037
Preprint. Discussion started: 18 June 2026

1991). They are associated with time-dependent loading in proximity to faults resulting from factors including static and dynamic stress changes and possible aseismic loading associated with slip or stress relaxation. Their complex spatiotemporal patterns differ widely from sequences that exhibit more steady background or swarm-like behavior, which are commonly associated with loading conditions such as pore-fluid pressure and tectonic loading transients (Hainzl, 2004; Shapiro et al., 1997; Essing & Poli, 2022; Lohman & McGuire, 2007). Quantifying the spatial and temporal clustering features of seismicity together with features of unclustered seismicity in a given region can provide insights into stress and loading conditions (Essing & Poli, 2024; Reverso et al., 2015; Zaliapin & Ben-Zion, 2020). We therefore use a nearest-neighbor approach to analyze clustering behavior and the background seismicity in the study area and interpret loading conditions on the spatiotemporal scale of notable sequences contained in the enhanced catalog (Baiesi & Paczuski, 2004; Zaliapin & Ben-Zion, 2013a). The nearest-neighbor approach links each event to its closest neighbor using a rescaled spatial and temporal distance between all event pairs. It helps separate earthquakes into background (Poisson distributed) and clustered seismicity, as well as quantify the sequential (swarm-like) or branch-like (mainshock-aftershock) behavior of clustered events.

The first step in the nearest-neighbor cluster analysis is to quantify the proximity of an event to its neighbors using pairwise distances between cataloged earthquakes (Baiesi & Paczuski, 2004; Zaliapin & Ben-Zion, 2013a). The proximity η between event i and consecutive event j can be written as:

$$\eta_{ij} = T_{ij} R_{ij} \quad (2).$$

Here η_{ij} consists of the two products, R_{ij} and T_{ij} , given by

$$T_{ij} = t_{ij} 10^{-pbm_i}; R_{ij} = \left(r_{ij}\right)^d 10^{-qbm_i} \quad (3),$$

where t_{ij} is the interevent time and r_{ij} the 3D spatial distance between event i and j. The fractal dimension d for 3D distances is set to 2.5 (Zaliapin & Ben-Zion, 2020), b is the b-value of the catalog, p and q = 0.5 (Zaliapin & Ben-Zion 2013a; Hsu et al., 2024), and m_i is the magnitude of event i. We use all events above M_c in our analysis. We estimate pairwise event distances in the η-space (Eq. 3) and statistically analyze the distances between nearest neighbors. We model the resulting bimodal distribution of nearest neighbor distances using a Gaussian-Mixture model to subsequently separate the two distributions (Martínez-Garzón et al., 2018; Fig. S4). Separating events in η-space isolates individual events that have large distances to their nearest neighbor (background) and identifies clusters of events that are closely connected to their nearest neighbors (clustered).

The resulting event clusters can be characterized by their topology, which is indicative of predominantly burst-like (branch-like) or swarm-like (sequential) sequences (Zaliapin & Ben-Zion, 2013b). Topology is quantified by a cluster's leaf depth, namely the number of events between the root (first) event and the last event of a branch of ancestors within a cluster. Small average leaf depth (d_m) values (< 5) indicate a short connection (i.e., increased influence) of the root event to the last event of a branch and is indicative of a branch-like cluster that suggests burst-like behavior. Large d_m values (≥ 5) indicate

https://doi.org/10.5194/egusphere-2026-3037
Preprint. Discussion started: 18 June 2026

comparatively long connections (i.e., less influence) between the root and last event of a branch that indicates a sequential cluster suggestive of swarm-like behavior (Zaliapin & Ben-Zion, 2013b).

4. Results

In the following, we first present the general results of catalog building and clustering characteristics that represent the broad features of the cataloged seismicity (Sections 4.1 and 4.2). We then present the largest sequences identified with the nearest-neighbor clustering, namely the Vartholomio and Zaharo sequences (Section 4.3).

4.1 Earthquake Catalog

The methodological analysis described in Section 2 yields an earthquake catalog encompassing seismicity from the entire study region (Fig. 2). As this study focuses specifically on crustal seismicity, we only consider events with hypocentral depths shallower than 1 km from the top of the slab (top of slab from Bocchini et al. (2018)). This threshold is chosen to effectively capture crustal-scale seismicity while minimizing contributions from deeper, intraslab and interplate events, which will be considered in subsequent studies. A comprehensive description of the catalog, including deeper seismicity, is provided in the Supplement Information (Text 2), and a focused discussion on intraslab seismicity is presented in Bocchini et al. (2026). The following then focuses on the upper plate earthquake distribution.

4.1.1. Seismicity in the Continental Crust

We restrict our catalog analysis to well-resolved locations with horizontal semi-major axis errors < 5 km, vertical errors < 5 km, and an RMS < 0.5, corresponding to average values of < 0.88 km horizontal error, < 0.78 km vertical error, and < 0.15 s in RMS (Fig. S9). Applying these filtering criteria leads to a total of 15,094 earthquakes with $-0.2 \leq M_L \leq 4.8$, $M_c = 0.9$, and b-value = 1.19±0.02 (Fig. 2c). The observed correlation between M_w - M_L follows the relation $M_w = 0.83\ M_L + 0.62$ (R-value = 0.97, Fig. 2d), which we use to convert M_L to M_0 in Fig. 4b (Kanamori & Brodsky, 2004).

In addition to the quality control criteria implemented in the workflow, we perform additional tests to ensure catalog solution robustness. First, we manually inspect waveforms from a sub-set of 100 random events and find no false detections. Second, we manually inspect the smallest-magnitude events in the catalog to ensure that they are consistent with typical locally recorded earthquake waveforms (Fig. S8). Third, we inspect the frequency-magnitude distribution (of the catalog subset of crustal events) and do not observe deviations from a power law (Fig. 2c; Fig. S6b). Fourth, we verify that the temporal evolution of the number of events in the catalog resembles the manually reviewed catalog published by the National Observatory of Athens (NOA), reflecting similar periods of increased and decreased seismicity (Fig. S6a). Notably, a quantitative comparison with the NOA catalog reveals a seven-fold increase in the number of detected events (Fig. S6a). Finally, we automatically scan the frequency domain of 2,639 newly detected events and fit their waveforms to a Boatwright

https://doi.org/10.5194/egusphere-2026-3037
Preprint. Discussion started: 18 June 2026

model during the M_w calculation for spurious outliers to flag errors of systematic false positive detections. We find no outliers that suggest false detections (Fig. 2d).

4.2 Seismicity Evolution

The enhanced catalog obtained in this study reveals significant seismicity rate changes (Fig. 3). Rates of tens of events per day persisted during first six months of the experiment (until May 2024) that were interrupted by short phases of comparatively higher rates (at ~2-week intervals) (Fig. 3a). For example, the daily number of events exceeded 100 events/day on 13 May 2024, with most events concentrated around the Zaharo area (Fig. 2a, b, yellow shaded). Rates remained elevated until 13 June 2024 and gradually returned to similar levels prior to May 2024. In a second period of increased activity, daily event counts concentrated around Vartholomio exceeded 200 events/day beginning on 6 July 2024 and lasted for ~8 days (Fig. 2a, b, purple shaded area).

The short time intervals between consecutive events (interevent times, IEs) in Fig. 3a with values as low as 10 s, reflect the catalog's high temporal resolution. Prior to May 2024, IEs maintain steady values between 10^3 – 10^4 s, where after August 2024, IEs vary sporadically and range between ~50 and 10,000 s, and averaged rates in May/June and July commonly drop below 1 hour. The seismicity evolution varies not only in time, but also in space, where seismicity rates are generally higher in the northern part of the study area (Fig. 3b). The general decrease from north to south is not gradual. It is overlain by earthquake clusters that are concentrated in space, and persistent for extended periods of time. Two spatially clustered groups of earthquakes are responsible for the < 1 hr IEs in May/June and July. One starts in mid-April 2024 (where the associated average IEs become apparent in June) at approximately 37.5°N. The cluster expands in space as well and increases in event rate over several weeks, peaks in activity in May 2024, and tapers out gradually in mid-August 2024. This sequence near Zaharo includes several events M_L > 2.5 (Fig. 2a; Fig. 3b). The second sequence begins relatively abruptly near 37.8°N at the beginning of July 2024, covers a comparatively large area relative to the Zaharo cluster, and decreases over several weeks. The two largest events in this cluster located near Vartholomio have M_L > 4 (Fig. 3b, Vartholomio). In section 4.3 we focus on the description of the nearest-neighbor clustering results of the two Zaharo and Vartholomio clusters to gain insight into the physical processes driving their evolution.

https://doi.org/10.5194/egusphere-2026-3037
Preprint. Discussion started: 18 June 2026

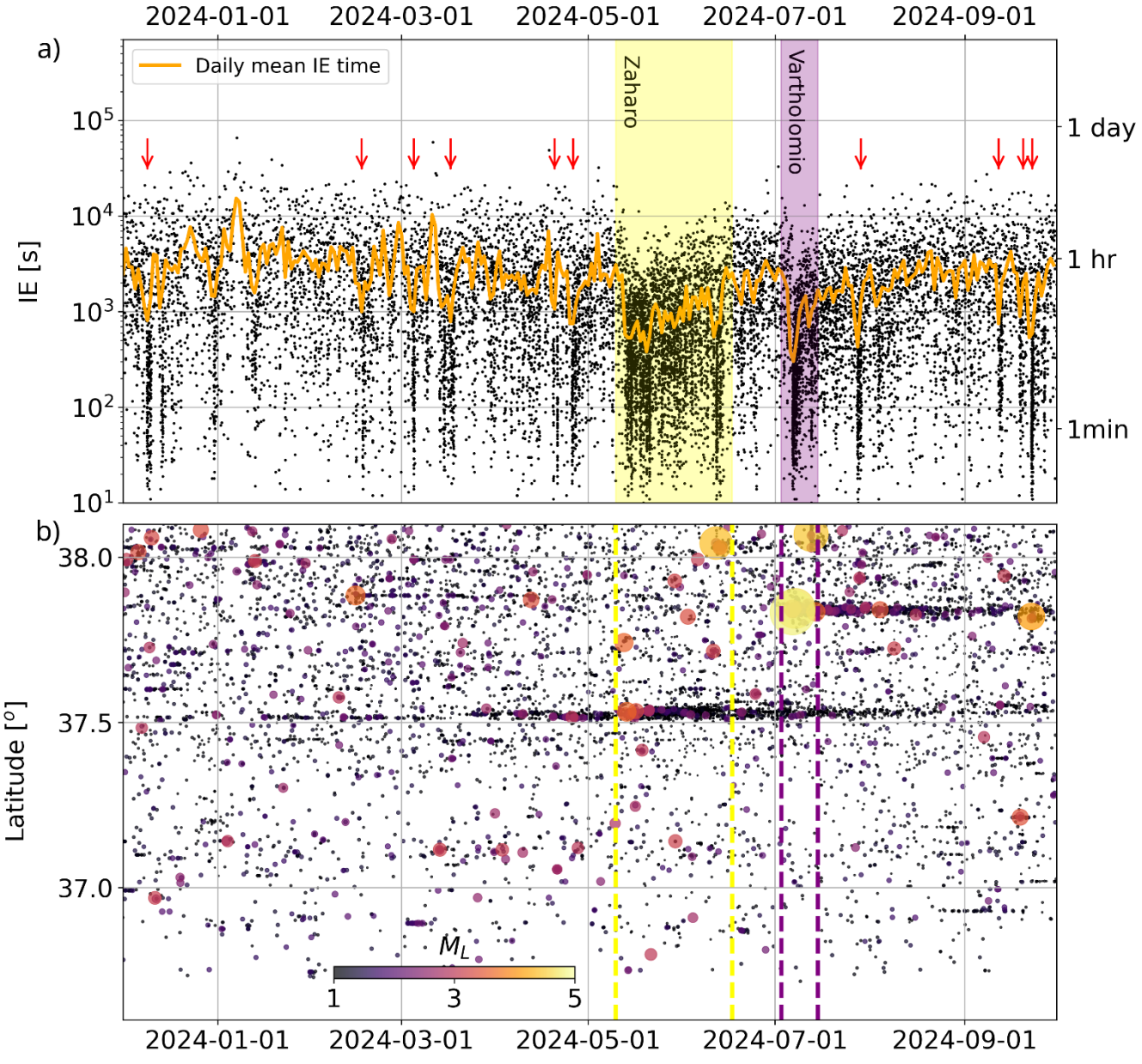

Figure 3: (a) Interevent times (IEs, black dots) and their daily average (orange line) as a function of time for crustal seismicity, where right y-axis shows the time intervals in minutes, hours, and days. Red arrows mark periods where the daily average drops below 10^3 s. (b) Spatio-temporal evolution of seismicity, color-coded and scaled according to M_L. Highlighted time periods correspond to the Zaharo (yellow) and the Vartholomio (purple) sequences as indicated in (a) and Fig. 2.

https://doi.org/10.5194/egusphere-2026-3037
Preprint. Discussion started: 18 June 2026

4.3 Nearest-Neighbor Clustering

The rescaled distances between nearest-neighbor event pairs in the space-time magnitude domain exhibits a bimodal distribution indicative of the presence of two general modes of seismicity within the study area that can be optimally separated with a value of $\eta = 3\times10^{-5}$ using a Gaussian Mixture Model (Fig. S4; Fig. 4a).

The following results and Discussion section treat the two populations individually. Nearest-neighbor pairs with large space-time distances follow a Poisson distribution that is consistent with background seismicity (Fig. 4b). In contrast, pairs with small distances are clustered into isolated pairs or groups of tens to hundreds of events (Fig. 4c), whose spatial organization reflects underlying stress conditions (Zaliapin & Ben-Zion, 2013b). Below we outline the characteristics of the background and organized (clustered) seismicity in the following two subsections.

4.3.1 Background Seismicity

Earthquake nearest-neighbor event pairs that fall above the $\eta = 3\times10^{-5}$ separation occur at a constant rate of approximately 4 events/day throughout the study period, as indicated with the red line of roughly constant slope in Fig. 4b. The seismicity rate and moment release are higher to the north relative to the south (Fig. 4b; Fig. S10). Background seismicity in the north concentrates primarily along the Movri fault, while locally confined background seismicity persists west of Pyrgos (Fig. S10).

4.3.2 Clustered Seismicity

The seismicity with rescaled distances that falls below the $\eta = 3\times10^{-5}$ separation is clustered, or organized, and with calculated average leaf depth (d_m) values that range from 2 (burst-like) to values of 17 (swarm-like) and cluster sizes that range from 2 to ~900 events (Fig. 4c). It is possible to quantify the separation between clusters with large numbers of events (> 100) based on the cluster size correlation as given by the leaf depth, d_m. For example, of the three clusters in the catalog that have > 100 events (Fig. 4c), Clusters 1 and 2 exhibit a strong correlation between d_m and cluster size, while Cluster 3 does not (Fig. 4c). The high correlation and high d_m suggests that Clusters 1 and 2 exhibit swarm-like behavior, and that Cluster 3 is more burst-like (Bocchini et al., 2022; Zaliapin & Ben-Zion, 2013b). All other clusters in the catalog with rescaled time and distance values below the η cutoff contain fewer than 100 events and are therefore excluded from further analysis.

Generally, clusters with small d_m and a lack of correlation with size tend to have the largest-magnitude events in the catalog (Fig. 4c). Conversely, clusters with large d_m tend to have gradual onsets that persist over time but contain comparatively smaller-magnitude events (Fig. 4c). As an example of the first cluster behavior (i.e., small d_m) clusters with $d_m < 5$ that appear uncorrelated with the number of events suggest a close connection between their respective ancestor events to the root event that is also indicative of a burst-like sequence. The largest events in such uncorrelated clusters tend to be among the larger-magnitude events. One prominent example is shown by the space-time evolution of the largest cluster, Cluster 3,

https://doi.org/10.5194/egusphere-2026-3037
Preprint. Discussion started: 18 June 2026

with ~ 900 events. Cluster 3 starts abruptly in early July and remains active for approximately two months (Fig. 4d, cluster 3). As an example of the second cluster behavior: d_m may be relatively large, which is consistent with increased independence between root and ancestor events, and is suggestive of a swarm-like sequence. The largest magnitude events in large d_m clusters generally fall in the range of smaller-magnitude events and their space-time evolution have gradual onsets with event rates that increase over time and remain active for several months (Fig. 4d, Cluster 1 & 2).

We now focus on the details of the most prominent sequences in greater detail, namely the Zaharo and Vartholomio sequences by examining their spatial and temporal patterns and focal mechanisms. For the cluster analysis, we also include events with $M_L < M_c$.

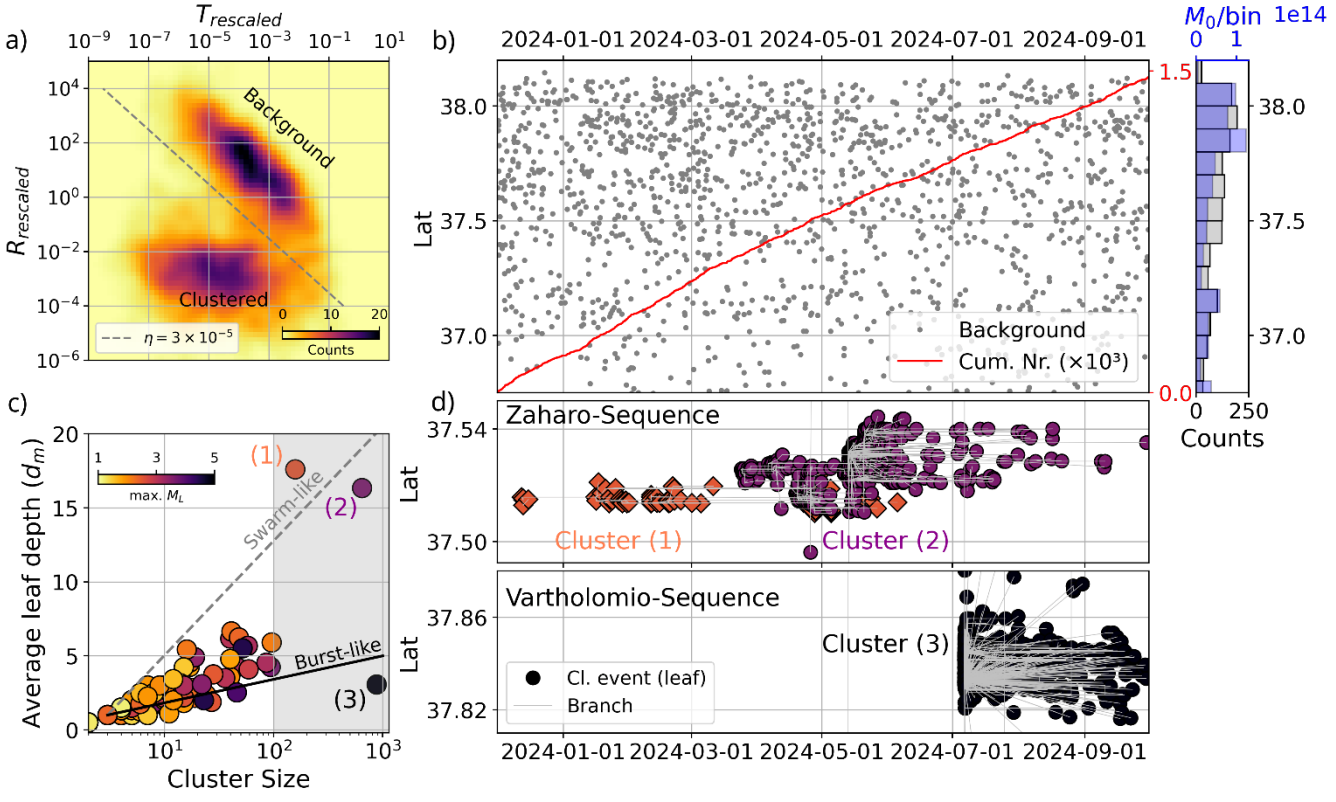

Figure 4: (a) Rescaled space Rij and time Tij distances between nearest neighbors ($M>M_c$) using df = 2.5, b = 1.19, p = 0.5, q = 0.5. (b) Cumulative number (Cum. Nr.) and spatiotemporal evolution of background seismicity. Seismicity rate and seismic moment (M_0) release in 0.1° bins showing a decrease from north to south. (c) Average leaf depth (d_m) as a function of cluster size color-coded by the maximum magnitude (M_L) for the clusters extracted from (a). (d) Spatiotemporal evolution of the three largest (> 100 events) clusters in (c).

4.4 Zaharo Sequence

Both Clusters 1 and 2 occur near Zaharo and concentrate in a dense, elongated ~6 km-long zone that strikes northwest-southeast and highlights a southwestward dipping plane with increasing complexity along strike towards southeast (Fig. 5). The normal-faulting focal mechanism of the largest event (M_L 3.6) has a nodal plane that is consistent with the seismicity

https://doi.org/10.5194/egusphere-2026-3037
Preprint. Discussion started: 18 June 2026

distribution (Fig. 5a, 5b; B–B′, C–C′). Hypocenter depths range between 6-8 km and highlight both the dip angle of the M_L 3.6 event, as well as fault planes dipping at steep angles to the northwest, quasi perpendicular to the strike of the M_L 3.6 event (Fig. 5b, A-A').

Seismicity in Cluster 1 starts at the beginning of the study period with increasing seismicity rates that are interrupted by periods of quiescence. Seismicity rates peak at the end of February and abate at the beginning of March (Fig. 5c). Seismicity related to Cluster 2 starts in mid-March with periods of high seismicity punctuated by intervals of lower activity (Fig. 5c). The largest event (M_L > 3) in Cluster 2 occurs in the latter part of the sequence in mid-May (Fig. 5c). In addition, seismicity appears to exhibit distinct migration patterns as the sequence evolves: short-range migration begins in Cluster 1 to the southeast (towards A' in Fig. 5a, c) at an apparent migration velocity of ~20 m d^{-1} and continues in the early stage of Cluster 2. In later stages of Cluster 2 (May 2024), migration proceeds to the northwest (towards A in Fig. 5a, c) at an apparent velocity of ~300 m d^{-1}. The regions activated during cluster migration remain active for weeks to months (Fig. 5c). The overall migration pattern (Fig. 5c) is also evident from the *Ts-Tp* times at a station (RP05) that is located along the strike of the cluster (Fig. S2; Fig. S11).

4.5 Vartholomio Sequence

Cluster 3 has a low d_m value that does not correlate with cluster size and contains two of the largest-magnitude earthquakes in the catalog. The largest events in Cluster 3 consist of two M_L > 4 strike-slip earthquakes, as indicated by their focal mechanisms, with hypocenters west of the town of Vartholomio (Fig. 6a). Data quality enabled inverting an MT solution for one additional M3.8 event that exhibits a similar kinematic pattern. Cluster 3 exhibits a 5 km long linear trend that strikes north-northeast and is parallel to one of the nodal planes common to the three MT solutions. Hypocentral depths are between 11-15 km and highlight a nearly vertical plane (Fig. 6b, B-B') that deepens along strike towards the south-southwest (Fig. 6b, A-A'). The sequence starts with a doublet of the two largest events (M_L = 4.8 on 2024-07-06, M_L = 4.7 on 2024-07-07) that occur 21 hours apart. The overall aftershock sequence exhibits a modified Omori-law *p*-value of 0.83. Following the initial seismicity rate decay after the two M > 4 events, the seismicity rate remains elevated for additional two months relative to rates preceding the sequence (Fig. 6c).

5. Interpretation and Discussion

The new enhanced catalog in the western Peloponnese built in this work for a ~10-month period in 2023/24 uses an aggregate network of permanent and temporary seismic stations and in this work, we focus on the crustal seismicity and its relation to shallow faults. The average interstation distance of 46.9 km and reduced M_c for crustal seismicity from 1.6 obtained from the national earthquake monitoring agency to 0.9 (Fig. 2c; Fig. S6c) highlights increased seismic activity near the towns of Pyrgos, Vartholomio, and Zaharo (Fig. 2a).

https://doi.org/10.5194/egusphere-2026-3037
Preprint. Discussion started: 18 June 2026

Nearest-neighbor clustering of the crustal seismicity reveals a decrease in background seismicity rates and seismic moment release from north to south, as well as isolated swarm-like clustering behavior and mainshock-aftershock sequences (Fig. 4). Variations in clustering behavior (swarm-like, burst-like) may reflect multiple loading mechanisms active within the study area, including event-event triggering or external processes like aseismic loading or pore-fluid pressure diffusion (Helmstetter et al., 2005; Kisslinger & Jones, 1991; Hainzl, 2004; Shapiro et al., 1997; Essing & Poli, 2022; Lohman & McGuire, 2007). Following Zaliapin & Ben-Zion (2013a, b), we separate the following discussion into background and clustered seismicity (Fig. 4a; Fig. S4), highlighting their distinct characteristics and implications for fault interactions and loading mechanisms.

5.1 Background Seismicity

Fluctuations in background seismicity rates typically indicate changes in large-scale tectonic forcing (Reverso et al., 2015). The largely constant background seismicity rate for the entire study region exhibits minor fluctuations that suggest that no significant changes in large-scale tectonic forcing occur during the observation period (Fig. 4b). We observe a decrease in background seismicity rates from 2 to 1 event per day from north to south (Fig. S10). The relatively higher background seismicity rates and moment release in the North compared to the South may result from differences in station coverage. However, since the nearest-neighbor analysis was conducted using events above M_c, potential effects of station coverage are likely negligible. The increased background seismicity rates therefore more likely reflect an increase in large-scale tectonic forcing and are consistent with the general northward increase in strain-rate that has been observed in several geodetic studies (Chousianitis et al., 2015; D'Agostino et al., 2020). Another notable feature of the background seismicity is that it appears spatially concentrated near a previously active fault. For example, Fig. S10 highlights an area of elevated background seismicity that follows the trace of the Movri fault that was active in the 2008 M_w Movri-sequence (Fig. 1; Serpetsidaki et al., 2014). Another example where background rates are elevated is seen in Fig. S10 near Pyrgos in an area that hosted a M_L 5.2 sequence in 1993 (Koukouvelas et al., 1996, Melis et al., 1994). In general, elevated rates of background seismicity near prominent fault structures are consistent with long-term accumulation of rock damage developing in a zone around major fault structures (Ben-Zion & Zaliapin, 2020).

5.2 Clustered Seismicity

Of the 454 event clusters identified by the nearest-neighbor analysis, the three largest clusters (N > 100) exhibit variable clustering behavior, as outlined in the results (Fig. 3; Fig. 4c). We first discuss the swarm-like behavior of the Zaharo sequences, followed by the burst-like clustering behavior of the Vartholomio sequence. We then consider the implications for possible loading conditions.

https://doi.org/10.5194/egusphere-2026-3037
Preprint. Discussion started: 18 June 2026

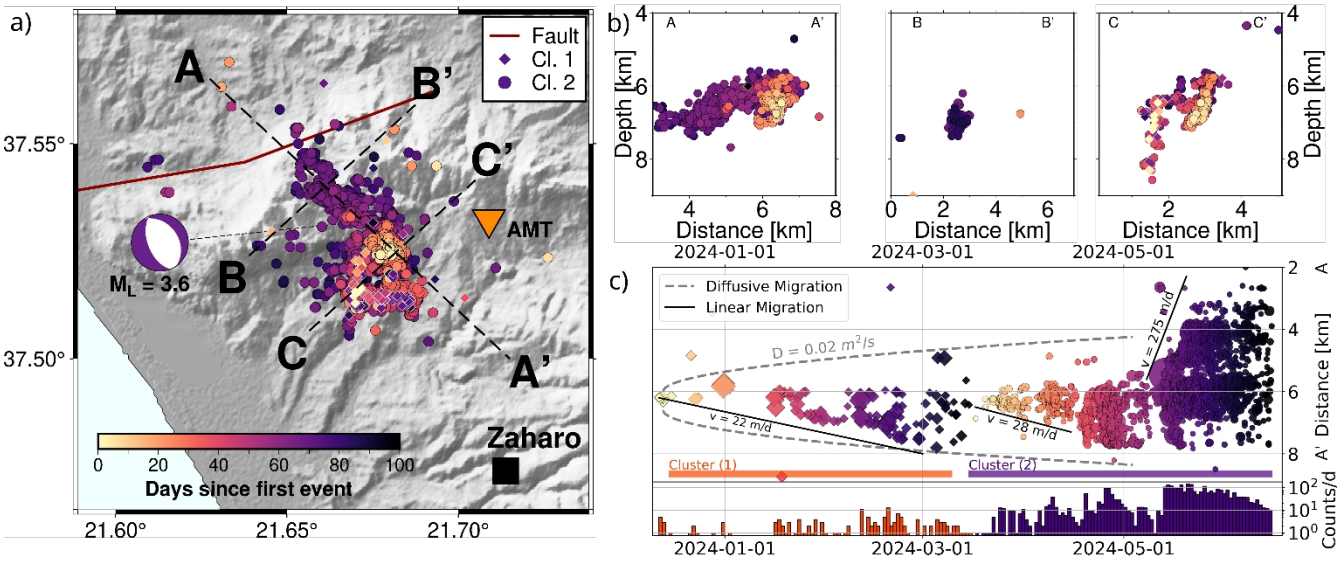

Figure 5: (a) Map view of seismicity related to Clusters 1 and 2 near Zaharo (black square). Orange triangle indicates the nearest seismic station. Seismicity is color-coded according to time relative to the first event in a sequence with diamonds (Cluster 1) and circles (Cluster 2). Dashed black lines indicate cross-sections. The largest event (M_L=3.6) is indicated by its focal mechanism. Red line indicates a mapped fault (DISS Working Group, 2021). (b) Cross-sections and color-coding according to (a). (c) Spatiotemporal evolution of seismicity projected along A-A' with histogram in counts per day. Horizontal bars indicate time periods of activity for Clusters 1 (orange) and 2 (purple) derived from nearest-neighbor clustering.

5.2.1 Zaharo Sequence

The long-lasting, productive sequence near the town of Zaharo differs from the Vartholomio sequence in multiple ways: (1) the largest earthquake (M3.6) occurs later in the sequence, and (2) the faulting style consists of normal faulting in the case of the Zaharo sequence. Both the seismicity and the MT solution deviate from the active, mapped faults with predominantly east-west strike (Lekkas et al., 2000; Papanikolaou et al. 2007, Mason et al., 2015), as well as from the extensional kinematics observed to the north in the Corinth rift (Pacchiani & Lyon-Caen, 2010; Fig. 2a; Fig. 5) both of which are consistent with north-south extension. The inferred strike of the structure activated by Clusters 1 and 2 is consistent with mapped faults southeast of Zaharo and with faults that were activated in the August 2011 sequence close to Oichalia, near Kalamata (Kassaras et al., 2014), suggesting northeast-southwest oriented extension (Fig. 1; Fig. 2a). The change in normal fault orientation from north to south suggests a change in the orientation of the extensional stress field from north to south near the Corinth rift to northeast-southwest near Zaharo. Rapid north-south extension within the Corinth rift is attributed to the combined effects of south-westward propagation of the North Anatolian fault tip and back-arc extension in the Hellenic subduction system (Armijo et al., 1996). In contrast, the northeast-southwest extension to the south as observed in Zaharo and Kalamata - orthogonal to the strike of the subducting slab of the Hellenic subduction system - may be driven mainly by gravitational collapse (Hatzfeld et al., 1997; Martinod et al., 2000) and/or slab rollback and associated trench retreat (Le Pichon et al., 1995). Geodetic and seismological studies also support the change of orientation of the extensional stress regime (Chousianitis et al., 2015; D'Agostino et al., 2020; Konstantinou et al., 2017; Lazos et al., 2025).

https://doi.org/10.5194/egusphere-2026-3037
Preprint. Discussion started: 18 June 2026

Another notable aspect of this sequence is the prominent swarm-like character, with features including: a persistent elevated seismicity rate (Fig. 4; Fig. 5), the lack of a clear large-magnitude mainshock (Fig. 3b; Fig. 4c), earthquakes that migrate at velocities consistent with typical crustal diffusivity values (Fig. 5; Fig. S11), a strong correlation between cluster size and d_m (Fig. 4c), and a *b*-value increase of 1.25±0.06 relative to the *b*-value of the Vartholomio sequence (1.1±0.07) (Fig. 2c). Similar swarm-like activity has not previously been reported in this area or its immediate surroundings, with the nearest example being in Oichalia, close to Kalamata, ~ 40 km to the southeast (Kassaras et al., 2014; Fig. 1, M_w 4.8 15. Aug. 2011) and in the Corinth rift (~90 km NE; Pacchiani & Lyon-Caen, 2010).

Commonly proposed driving mechanisms for swarm-like sequences with similar characteristics include factors such as pore-fluid pressure diffusion (Shapiro et al., 1997; Hainzl, 2004) and aseismic loading (Essing & Poli, 2022; Lohman & McGuire, 2007; Martínez-Garzón et al., 2021). While often proposed separately, recent studies have shown that triggering by aseismic loading can be facilitated by elevated pore-fluid pressure that reduces the effective normal stress and subsequently leads to dilational strengthening (Guglielmi et al., 2015). In such cases, the pore pressure evolution that leads to the initial swarm-like behavior may evolve such that if potentially dynamic rupture were to initiate, dilational strengthening may lead eventually to rupture arrest before it becomes unstable. The associated microseismicity that accompanies aseismic slip transients would then migrate at speeds governed by the aseismic slip (Guglielmi et al., 2015; Danré et al., 2022; De Barros et al., 2021). In other words, the time scales involved in the migration of small earthquakes can provide additional (indirect) indications on the primary driving mechanism (Danré et al., 2024).

If the initial part of the sequence is driven by pore-pressure diffusion, it begs the question of plausible sources of fluid influx. Fluids are reported to be released from the downgoing Nubian plate and that migrate upward into the continental crust (Halpaap et al., 2019). Faults in the overriding crust may then serve as conduits facilitating upward penetration (Caine et al., 1996; Shipton et al., 2004). Surface manifestations of the presence of fluids in the crust include thermal springs near the town of Zaharo (Kiskyras, 1962), and seismic swarms, such as the one near Kalamata that has previously been interpreted as being linked to fluid diffusion (Kassaras et al., 2014). The migration of seismicity outward from the center of the A-A' cross section in Fig. 5 progresses at speeds that are consistent with the range commonly observed for crustal diffusivity values (Scholz, 2019; Shapiro et al., 1997). Notably, Cluster 1 migrates southeastward at velocities of ~20 m d^{-1} at a similar velocity as observed for a swarm in California (Ross et al., 2020). Seismicity in the early phase of the activity of Cluster 2 proceeds to migrate at similar speeds and directions until approximately the last week of April, after which, the migration speed abruptly increases by an order of magnitude to ~300 m d^{-1} with a simultaneous uptick in the event rate. This rapid increase of migration speed and event rate in the first week of May highlights a rapid change of behavior of the seismicity that could suggest a change in driving mechanism. This change in behavior could reflect a pressure-driven acceleration of slip at aseismic speeds. It may also reflect a transition in diffusion properties or shift of deformation onto a neighboring fault to northwest. The sudden shift in migration speed is abrupt, but still consistent with swarm migration velocities that are proposed to be related to pore fluid pressure diffusion (De Barros et al., 2020; Duverger et al., 2018). Whether migration velocities reach typical values in the order of km d^{-1} that are commonly inferred to be a sign of aseismic loading (De Barros

https://doi.org/10.5194/egusphere-2026-3037
Preprint. Discussion started: 18 June 2026

et al., 2020) is difficult to resolve with the current catalog. Future work in the Zaharo region will use a local velocity model and coherence-based detection methods (i.e., template matching) to enhance the catalog and refine our estimates of migration velocities with aim to investigate the sudden change in migration speeds. Nevertheless, the current resolution appears to highlight a rapid change of earthquake migration behaviour that suggests a change in the driving mechanism which currently might be easily explained with a potential acceleration of (aseismic) slip.

5.2.2 Vartholomio Sequence and Surroundings

The burst-like behavior of the Vartholomio sequence inferred from the weak correlation between cluster size and d_m (Fig. 4c) and the consistency of the MT solutions and aftershock distribution, suggest a mainshock-aftershocks sequence driven by tectonic loading. The interpretation is supported by the fact that the inferred faults are optimally oriented for failure in the local ambient stress field that is dominated by southwest oriented horizontal compressional stress as suggested by geodetic observations (Lazos et al., 2025). While tectonic loading may be the primary driving mechanism for the Vartholomio cluster, there may still be evidence of fluid-driven earthquake interactions. The protracted temporal length of the aftershock seismicity in the Vartholomio sequence (Fig. 6), also evident from the relatively small, modified Omori-Law *p*-value (0.83), is consistent with fluid-driven prolongation of aftershock activity. Elevated aftershock rates can be related to fluid-saturated areas (Ross et al., 2017), where pore-fluid pressure diffusion triggers aftershock seismicity (Miller, 2020). While observations of shallow thermal fluids in vicinity to Vartholomio would support the above interpretation (Lambrakis & Kallergis, 2005), the effect at depths > 10 km remains unclear, and would also be the subject of future catalog enhancement work.

The spatial distribution of the Vartholomio sequence aligns with one of the nodal planes common for all three moment tensors indicating a right-lateral sense of motion which is in agreement with the kinematics of the 8 June 2008 Movri sequence that occurred ~ 30 km northeast of Vartholomio (Ganas et al., 2009; Serpetsidaki et al., 2014; Fig. 1), as well as with the strike of the Kefalonia transform fault that lies ~ 80 km to the northwest (Kiratzi & Louvari, 2003 ; Fig. 2a). The right lateral kinematic observations from this and previous work (e.g., Serpetsidaki et al., 2010) suggest similar right lateral kinematics for strike slip events in this area akin to the 16 October 1988 earthquake for which the sense of motion could not be resolved (Fig. 1; Feng et al., 2010; Kiratzi & Louvari, 2003). It is possible that the right-lateral slip may be distributed over several faults in a diffuse fault zone between the Movri fault westward and the coast line (Feng et al., 2010). In summary, the clustering behavior of this sequence is broadly consistent with being driven by tectonic loading and stress interactions within a diffuse right-lateral strike-slip fault system that may define a diffuse boundary at the southern edge of the Ionian-Akarnania Block (Haddad et al., 2020).

https://doi.org/10.5194/egusphere-2026-3037
Preprint. Discussion started: 18 June 2026

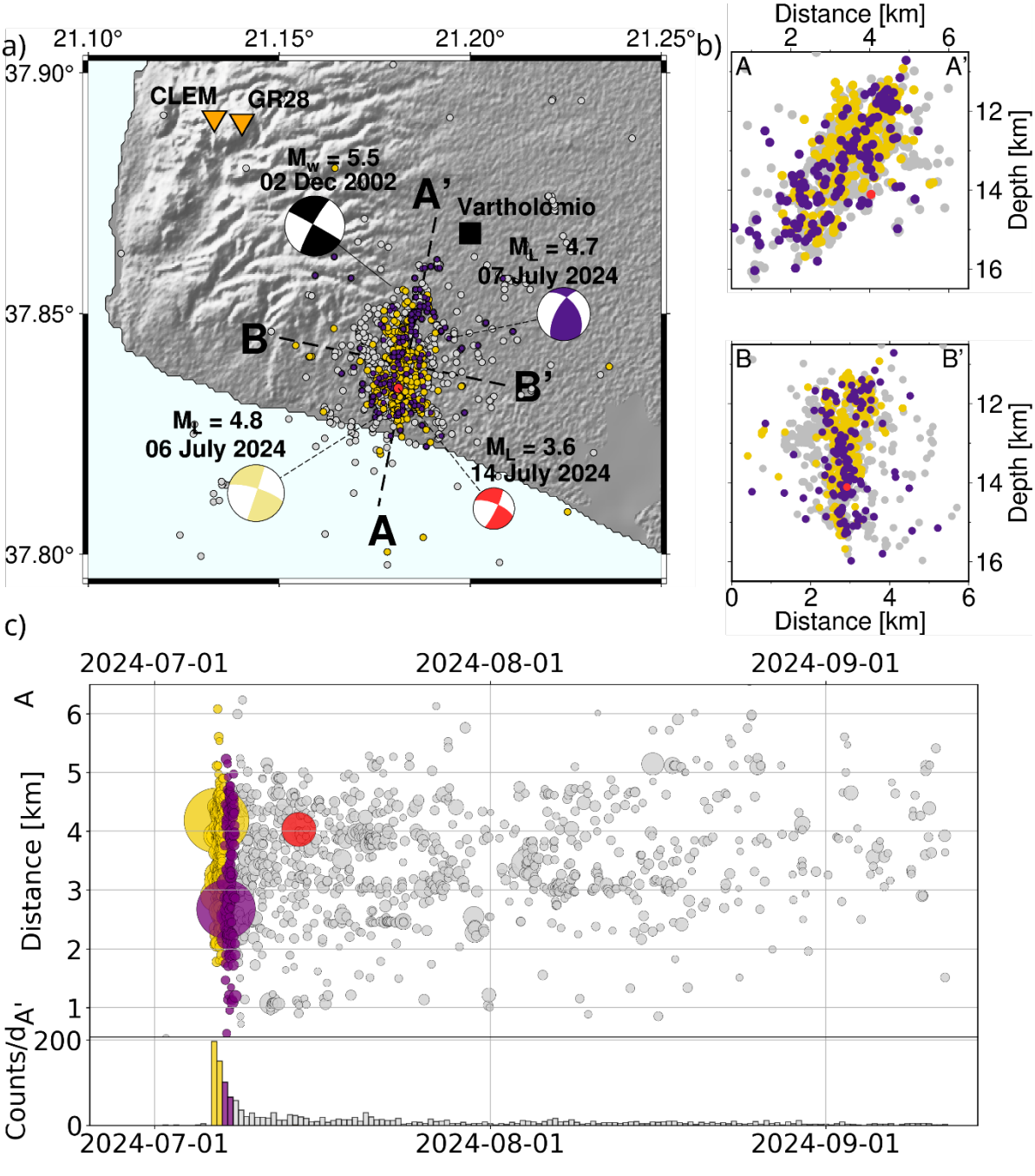

Figure 6: (a) Map view of Cluster 3 seismicity near Vartholomio (black square). Orange triangles indicate two closest seismic stations and yellow and purple dots indicate the earthquakes in the first 21/24 hours after the respective mainshocks with the same color coding in map (a) and cross-sectional (b) views. Focal mechanisms for the three largest events in this sequence exhibit similar, common nodal planes consistent with the distribution of aftershocks (yellow, purple). Black focal mechanism is from the 2 December 2002 earthquake (M_w = 5.5) from Serpetsidaki et al., (2010), and exhibits a similar deformation style. (b) Cross-sections and color-coding according to (a). (c) Spatiotemporal evolution of seismicity projected along A-A' and its temporal evolution in counts per day with color-coding as the focal mechanism in (a).

https://doi.org/10.5194/egusphere-2026-3037
Preprint. Discussion started: 18 June 2026

6. Conclusion

In this study, we use an integrated set of existing and new data from seismic stations in western Greece to obtain a high-resolution earthquake catalog spanning 10 months from December 2023 until September 2024, with focus on the shallow seismicity. Our analysis leads to 15,094 high-quality events in the upper plate, and we are able to decrease the magnitude of completeness, M_c, from 1.6 to 0.9. Background seismicity, extracted from a nearest-neighbor clustering approach, exhibits a decrease in average rate of 2 to 1 per day from north to south, and is consistent with observed changes in the stressing rate as inferred by geodetic studies. Nearest-neighbor clustering analysis also reveals significant seismic sequences near the towns of Zaharo and Vartholomio with variable behavior inferred from statistical and spatiotemporal migration properties. The two clusters in the Zaharo sequence lead to two main conclusions: 1) the orientation of maximum extensional stress changes from north-south near the Corinth rift to east-west near Zaharo, which is consistent with stress orientation and fault orientations that have been inferred to be associated with slab rollback and trench retreat to the south. 2) The temporal evolution of migration patterns within the two clusters are consistent with crustal diffusivity values, where a sudden acceleration of seismicity migration suggests a change in driving mechanism, possibly related to an aseismic loading transient. Both mechanisms are consistent with fluid-rock interactions that would be supported by the presence of geothermal activity in the vicinity and an upward migration of fluids that may originate from slab-dewatering. In contrast, the observed right-lateral strike-slip kinematics in the Vartholomio mainshock-aftershock sequence are consistent with the stress field loading that drives the deformation along the Movri fault and structures that have hosted previous earthquakes in the area (2 December 2002). The sequence may host deformation in a diffuse zone that is thought to accommodate right lateral slip in a distributed region spanning the Movri fault, westward towards the Ionian Sea.

Finally, this study demonstrates how high-resolution seismicity catalogs enable studying earthquake interactions to a greater level of detail that help gain insights into a heterogeneous stress field and the coexistence of multiple end member faulting styles in proximity. Such detailed spatial and kinematic information is essential for understanding upper crustal deformation in subduction zones, which may pose a significant seismic hazard due to frequent, shallow earthquakes, potentially exceeding the hazard from less frequent but larger megathrust events.

Code and data availability

Maps were created using GMT 6.0 (Wessel et al., 2019) and PyGMT (Uieda et al., 2021). Seismic data were processed with ObsPy (Beyreuther et al., 2010). Event detection was performed using PhaseNet (Zhu & Beroza, 2019) and the Seisbench framework (Woollam et al., 2022), while phase association was performed using PyOcto (Münchmeyer, 2023). We estimate the parameters of the modified Omori-law using Goebel et al. (2019). Earthquake catalogs produced and analyzed in this study are available from Bocchini et al. (2025).

https://doi.org/10.5194/egusphere-2026-3037
Preprint. Discussion started: 18 June 2026

Supplement link

The link to the supplement will be included by Copernicus, if applicable.

Author contributions

DE: conceptualization, investigation, formal analysis, methodology, visualization, writing (original draft), validation. GMB: conceptualization, investigation, methodology, writing (review and editing), validation. MPR: methodology, data curation, writing (review and editing). AS: methodology, writing (review and editing). IN: methodology, writing (review and editing). RMH: conceptualization, writing (review and editing), funding acquisition. ES: conceptualization, writing (review and editing).

Competing interests

The authors acknowledge that there are no conflicts of interest.

Disclaimer

Copernicus Publications adds a standard disclaimer: “Copernicus Publications remains neutral with regard to jurisdictional claims made in the text, published maps, institutional affiliations, or any other geographical representation in this paper. While Copernicus Publications makes every effort to include appropriate place names, the final responsibility lies with the authors. Views expressed in the text are those of the authors and do not necessarily reflect the views of the publisher.”
Please feel free to add disclaimer text at your choice, if applicable.

Acknowledgements

The authors thank Anthony Lomax for his support with NLL-SSST-coherence. The authors thank the National Observatory of Athens for maintaining and publicly distributing their seismic stations and their earthquake catalog.

Financial support

This work was supported in part by overhead funding from the Deutsche ForschungsGemeinschaft (German Research Foundation), as well as research stipend money for the Earthquake Processes working group at the Ruhr University of Bochum.

https://doi.org/10.5194/egusphere-2026-3037
Preprint. Discussion started: 18 June 2026

Review statement

The review statement will be added by Copernicus Publications listing the handling editor as well as all contributing referees according to their status anonymous or identified.

References

Abercrombie, R. E. (1995). Earthquake source scaling relationships from− 1 to 5 ML using seismograms recorded at 2.5-km depth. Journal of Geophysical Research: Solid Earth, 100(B12), 24015-24036.

Armijo, R., Lyon-Caen, H., & Papanastassiou, D. (1991). A possible normal-fault rupture for the 464 BC Sparta earthquake. Nature, 351(6322), 137-139.

Armijo, R., Meyer, B. G. C. P., King, G. C. P., Rigo, A., & Papanastassiou, D. (1996). Quaternary evolution of the Corinth Rift and its implications for the Late Cenozoic evolution of the Aegean. Geophysical Journal International, 126(1), 11-53.

Aristotle University of Thessaloniki. (1981). Aristotle University of Thessaloniki Seismological Network [Data set]. International Federation of Digital Seismograph Networks. https://doi.org/10.7914/SN/HT

Avallone, A., Briole, P., Agatza-Balodimou, A. M., Billiris, H., Charade, O., Mitsakaki, C., ... & Veis, G. (2004). Analysis of eleven years of deformation measured by GPS in the Corinth Rift Laboratory area. *Comptes Rendus. Geoscience*, *336*(4-5), 301-311.

Baiesi, M., & Paczuski, M. (2004). Scale-free networks of earthquakes and aftershocks. Physical Review E—Statistical, Nonlinear, and Soft Matter Physics, 69(6), 066106.

Baltay, A., & Abercrombie, R. E. (2025). Seismic Moment and Local Magnitude Scales in Ridgecrest, California, from the SCEC/USGS community stress drop validation study. Bulletin of the Seismological Society of America, 115(3), 1279-1293.

Ben-Zion, Y. (2008). Collective behavior of earthquakes and faults: Continuum-discrete transitions, progressive evolutionary changes, and different dynamic regimes. Reviews of Geophysics, 46(4).

Ben-Zion, Y., & Zaliapin, I. (2020). Localization and coalescence of seismicity before large earthquakes. Geophysical Journal International, 223(1), 561-583.

Bindi, D., Spallarossa, D., Picozzi, M., & Morasca, P. (2020). Reliability of source parameters for small events in central Italy: Insights from spectral decomposition analysis applied to both synthetic and real data. Bulletin of the Seismological Society of America, 110(6), 3139-3157.

Bird, P. (2003). An updated digital model of plate boundaries. Geochemistry, Geophysics, Geosystems, 4(3).

Boatwright, J. (1980). A spectral theory for circular seismic sources; simple estimates of source dimension, dynamic stress drop, and radiated seismic energy. Bulletin of the Seismological Society of America, 70(1), 1-27.

Bocchini, G. M., Brüstle, A., Becker, D., Meier, T., Van Keken, P. E., Ruscic, M., ... & Friederich, W. (2018). Tearing, segmentation, and backstepping of subduction in the Aegean: New insights from seismicity. Tectonophysics, 734, 96-118.

https://doi.org/10.5194/egusphere-2026-3037
Preprint. Discussion started: 18 June 2026

Bocchini, G. M., Martínez-Garzón, P., Verdecchia, A., Harrington, R. M., Bohnhoff, M., Turkmen, T., & Nurlu, M. (2022). Direct evidence of a Slow-Slip Transient modulating the spatiotemporal and frequency-magnitude Earthquake distribution: Insights from the Armutlu Peninsula, Northwestern Turkey. Geophysical Research Letters, 49(18), e2022GL099077.

Bocchini, G. M., Essing, D., & Roth, M. (2025). High-resolution earthquake catalog and focal mechanism solutions for the western Hellenic subduction system (Greece) [Data set]. Zenodo. https://doi.org/10.5281/zenodo.17641018

Bocchini, G. M., Essing, D., Nikolopoulou, I., Dielforder, A., Roth, M. P., Serpetsidaki, A., ... & Harrington, R. M. (2026). Stress field and megathrust strength in the western Hellenic Subduction System: Insights from the 2024 Mw 5.9 Strofades earthquake sequence, Greece. *Geophysical Research Letters*, *53*(9), e2026GL122817.

Briole, P., Rigo, A., Lyon-Caen, H., Ruegg, J. C., Papazissi, K., Mitsakaki, C., ... & Deschamps, A. (2000). Active deformation of the Corinth rift, Greece: results from repeated Global Positioning System surveys between 1990 and 1995. *Journal of Geophysical Research: Solid Earth*, *105*(B11), 25605-25625.

Brune, J. N. (1970). Tectonic stress and the spectra of seismic shear waves from earthquakes. Journal of geophysical research, 75(26), 4997-5009.

Caine, J. S., Evans, J. P., & Forster, C. B. (1996). Fault zone architecture and permeability structure. Geology, 24(11), 1025-1028.

Chousianitis, K., Ganas, A., & Evangelidis, C. P. (2015). Strain and rotation rate patterns of mainland Greece from continuous GPS data and comparison between seismic and geodetic moment release. Journal of Geophysical Research: Solid Earth, 120(5), 3909-3931.

Cocard, M., Kahle, H. G., Peter, Y., Geiger, A., Veis, G., Felekis, S., ... & Billiris, H. (1999). New constraints on the rapid crustal motion of the Aegean region: recent results inferred from GPS measurements (1993–1998) across the West Hellenic Arc, Greece. Earth and Planetary Science Letters, 172(1-2), 39-47.

Corinth Rift Laboratory Team And RESIF Datacenter. (2013). CL - Corinth Rift Laboratory Seismological Network (CRLNET) [Data set]. RESIF - Réseau Sismologique et géodésique Français. https://doi.org/10.15778/RESIF.CL

Crosetto, S., Faccenna, C., Ballato, P., Mouslopoulou, V., Begg, J., Shen, C. C., & Hu, H. M. (2025). Kinematic evolution of the Cephalonia-Lefkada transform fault zone: Strain partitioning in response to subduction margin dynamics. Tectonics, 44(10), e2025TC008862.

d'Agostino, N., Métois, M., Koci, R., Duni, L., Kuka, N., Ganas, A., ... & Kandić, R. (2020). Active crustal deformation and rotations in the southwestern Balkans from continuous GPS measurements. Earth and Planetary Science Letters, 539, 116246.

Danré, P., De Barros, L., Cappa, F., & Ampuero, J. P. (2022). Prevalence of aseismic slip linking fluid injection to natural and anthropogenic seismic swarms. Journal of Geophysical Research: Solid Earth, 127(12), e2022JB025571.

Danré, P., De Barros, L., Cappa, F., & Passarelli, L. (2024). Parallel dynamics of slow slips and fluid-induced seismic swarms. Nature Communications, 15(1), 8943.

https://doi.org/10.5194/egusphere-2026-3037
Preprint. Discussion started: 18 June 2026

De Barros, L., Cappa, F., Deschamps, A., & Dublanchet, P. (2020). Imbricated aseismic slip and fluid diffusion drive a seismic swarm in the Corinth Gulf, Greece. Geophysical Research Letters, 47(9), e2020GL087142.

De Barros, L., Wynants-Morel, N., Cappa, F., & Danré, P. (2021). Migration of fluid-induced seismicity reveals the seismogenic state of faults. Journal of Geophysical Research: Solid Earth, 126(11), e2021JB022767.

DISS Working Group, 2021. Database of Individual Seismogenic Sources (DISS), Version 3.3.0: a compilation of potential sources for earthquakes larger than M 5.5 in Italy and surrounding areas. Istituto Nazionale di Geofisica e Vulcanologia (INGV). https://doi.org/10.13127/diss3.3.0.

Duverger, C., Lambotte, S., Bernard, P., Lyon-Caen, H., Deschamps, A., & Nercessian, A. (2018). Dynamics of microseismicity and its relationship with the active structures in the western Corinth Rift (Greece). Geophysical Journal International, 215(1), 196-221.

Essing, D., & Poli, P. (2022). Spatiotemporal evolution of the seismicity in the alto tiberina fault system revealed by a high-resolution template matching catalog. Journal of Geophysical Research: Solid Earth, 127(10), e2022JB024845.

Essing, D., & Poli, P. (2024). Unraveling earthquake clusters composing the 2014 Alto Tiberina earthquake swarm via unsupervised learning. Journal of Geophysical Research: Solid Earth, 129(1), e2022JB026237.

Felzer, K. R., Abercrombie, R. E., & Ekstrom, G. (2004). A common origin for aftershocks, foreshocks, and multiplets. Bulletin of the Seismological Society of America, 94(1), 88-98.

Feng, L., Newman, A. V., Farmer, G. T., Psimoulis, P., & Stiros, S. C. (2010). Energetic rupture, coseismic and post-seismic response of the 2008 MW 6.4 Achaia-Elia Earthquake in northwestern Peloponnese, Greece: an indicator of an immature transform fault zone. Geophysical Journal International, 183(1), 103-110.

Freed, A. M. (2005). Earthquake triggering by static, dynamic, and postseismic stress transfer. Annu. Rev. Earth Planet. Sci., 33(1), 335-367.

Friederich W., Evangelidis C., Papazachos C., Sokos E., Kaviris G., & Cernih G.. (2022). AdriaArray Temporary Network: Greece, North Macedonia [Data set]. International Federation of Digital Seismograph Networks. https://doi.org/10.7914/Y0T2-3B67

Gallovič, F., Zahradník, J., Křížová, D., Plicka, V., Sokos, E., Serpetsidaki, A., & Tselentis, G. A. (2009). From earthquake centroid to spatial-temporal rupture evolution: Mw 6.3 Movri Mountain earthquake, June 8, 2008, Greece. Geophysical Research Letters, 36(21).

Ganas, A., Serpelloni, E., Drakatos, G., Kolligri, M., Adamis, I., Tsimi, C., & Batsi, E. (2009). The Mw 6.4 SW-Achaia (Western Greece) earthquake of 8 June 2008: seismological, field, GPS observations, and stress modeling. Journal of Earthquake Engineering, 13(8), 1101-1124.

Gao, D., Kao, H., & Wang, B. (2021). Misconception of waveform similarity in the identification of repeating earthquakes. Geophysical Research Letters, 48(13), e2021GL092815.

https://doi.org/10.5194/egusphere-2026-3037
Preprint. Discussion started: 18 June 2026

Geller, R. J., & Mueller, C. S. (1980). Four similar earthquakes in central California. Geophysical Research Letters, 7(10), 821-824.

Goebel, T. H. W., Rosson, Z., Brodsky, E. E., & Walter, J. I. (2019). Aftershock deficiency of induced earthquake sequences during rapid mitigation efforts in Oklahoma. Earth and Planetary Science Letters, 522, 135-143.

Guglielmi, Y., Cappa, F., Avouac, J. P., Henry, P., & Elsworth, D. (2015). Seismicity triggered by fluid injection–induced aseismic slip. Science, 348(6240), 1224-1226.

Haddad, A., Ganas, A., Kassaras, I., & Lupi, M. (2020). Seismicity and geodynamics of western Peloponnese and central Ionian Islands: Insights from a local seismic deployment. Tectonophysics, 778, 228353.

Halpaap, F., Rondenay, S., Perrin, A., Goes, S., Ottemöller, L., Austrheim, H., ... & Eeken, T. (2019). Earthquakes track subduction fluids from slab source to mantle wedge sink. Science Advances, 5(4), eaav7369.

Hanks, T. C., & Boore, D. M. (1984). Moment-magnitude relations in theory and practice. Journal of Geophysical Research: Solid Earth, 89(B7), 6229-6235.

Hainzl, S. (2004). Seismicity patterns of earthquake swarms due to fluid intrusion and stress triggering. Geophysical Journal International, 159(3), 1090-1096.

Harrington, R. M.,Bocchini, G. M.,Roth, M. P., Sokos E., & Evangelidis, C. (2023). RUB Observational Geophysics Lab Deployment: Northwestern Peloponnese [Data set]. International Federation of Digital Seismograph Networks. https://doi.org/10.7914/pxkt-x819

Hatzfeld, D., Pedotti, G., Hatzidimitriou, P., & Makropoulos, K. (1990). The strain pattern in the western Hellenic arc deduced from a microearthquake survey. Geophysical Journal International, 101(1), 181-202.

Hatzfeld, D., Martinod, J., Bastet, G., & Gautier, P. (1997). An analog experiment for the Aegean to describe the contribution of gravitational potential energy. Journal of Geophysical Research: Solid Earth, 102(B1), 649-659.

Helmstetter, A., Kagan, Y. Y., & Jackson, D. D. (2005). Importance of small earthquakes for stress transfers and earthquake triggering. Journal of Geophysical Research: Solid Earth, 110(B5).

Hsu, Y. F., Zaliapin, I., & Ben-Zion, Y. (2024). Informative modes of seismicity in nearest-neighbor earthquake proximities. Journal of Geophysical Research: Solid Earth, 129(3), e2023JB027826.

Hutton, L. K., & Boore, D. M. (1987). The ML scale in southern California. Bulletin of the Seismological Society of America, 77(6), 2074-2094.

Kagan, Y. Y. (1991). 3-D rotation of double-couple earthquake sources. Geophysical Journal International, 106(3), 709-716.

Kanamori, H., & Brodsky, E. E. (2004). The physics of earthquakes. Reports on progress in physics, 67(8), 1429.

Kassaras, I., Kapetanidis, V., Karakonstantis, A., Kouskouna, V., Ganas, A., Chouliaras, G., ... & Makropoulos, K. (2014). Constraints on the dynamics and spatio-temporal evolution of the 2011 Oichalia seismic swarm (SW Peloponnesus, Greece). Tectonophysics, 614, 100-127.

Kassaras, I., Kapetanidis, V., & Karakonstantis, A. (2016). On the spatial distribution of seismicity and the 3D tectonic stress field in western Greece. Physics and Chemistry of the Earth, Parts A/B/C, 95, 50-72.

https://doi.org/10.5194/egusphere-2026-3037
Preprint. Discussion started: 18 June 2026

Kiratzi, A., & Louvari, E. (2003). Focal mechanisms of shallow earthquakes in the Aegean Sea and the surrounding lands determined by waveform modelling: a new database. Journal of Geodynamics, 36(1-2), 251-274.

Kiskyras, D. A. (1962). The mineral springs of Peloponnesus. Peloponnesian New Years, 103-109.

Kisslinger, C., & Jones, L. M. (1991). Properties of aftershock sequences in southern California. Journal of Geophysical Research: Solid Earth, 96(B7), 11947-11958.

Koukouvelas, I., Mpresiakas, A., Sokos, E., & Doutsos, T. (1996). The tectonic setting and earthquake ground hazards of the 1993 Pyrgos earthquake, Peloponnese, Greece. Journal of the Geological Society, 153(1), 39-49.

Konstantinou, K. I., & Melis, N. S. (2018). The relationship between local and moment magnitude in Greece during the period 2008–2016. Pure and Applied Geophysics, 175, 731-740.

Konstantinou, K. I., Mouslopoulou, V., Liang, W. T., Heidbach, O., Oncken, O., & Suppe, J. (2017). Present-day crustal stress field in Greece inferred from regional-scale damped inversion of earthquake focal mechanisms. Journal of Geophysical Research: Solid Earth, 122(1), 506-523.

Lambrakis, N., & Kallergis, G. (2005). Contribution to the study of Greek thermal springs: hydrogeological and hydrochemical characteristics and origin of thermal waters. Hydrogeology Journal, 13(3), 506-521.

Lazos, I., Sboras, S., Kokkalas, S., Karastathis, V., Xiroudakis, G., Iordanidou, K., ... & Pavlides, S. (2025). Seismotectonic implications for the Peloponnese (SW Greece) region based on geodetic crustal deformation analysis. Tectonophysics, 230969.

Lekkas, E., Fountoulis, L. & Papanikolaou, D. (2000): Intensity Distribution and Neotectonic Macrostructure Pyrgos Earthquake Data (26 March 1993, Greece). – Natural Hazards 21: 19–33.

Le Pichon, X., Chamot-Rooke, N., Lallemant, S., Noomen, R., & Veis, G. (1995). Geodetic determination of the kinematics of central Greece with respect to Europe: Implications for eastern Mediterranean tectonics. Journal of Geophysical Research: Solid Earth, 100(B7), 12675-12690.

Lohman, R. B., & McGuire, J. J. (2007). Earthquake swarms driven by aseismic creep in the Salton Trough, California. Journal of Geophysical Research: Solid Earth, 112(B4).

Lomax, A., Virieux, J., Volant, P., & Berge-Thierry, C. (2000). Probabilistic earthquake location in 3D and layered models: Introduction of a Metropolis-Gibbs method and comparison with linear locations. In Advances in seismic event location (pp. 101-134). Dordrecht: Springer Netherlands.

Lomax, A., & Savvaidis, A. (2022). High-precision earthquake location using source-specific station terms and inter-event waveform similarity. Journal of Geophysical Research: Solid Earth, 127(1), e2021JB023190.

Louvari, E., Kiratzi, A. A., & Papazachos, B. C. (1999). The Cephalonia transform fault and its extension to western Lefkada Island (Greece). Tectonophysics, 308(1-2), 223-236.

Martínez-Garzón, P., Zaliapin, I., Ben-Zion, Y., Kwiatek, G., & Bohnhoff, M. (2018). Comparative study of earthquake clustering in relation to hydraulic activities at geothermal fields in California. Journal of Geophysical Research: Solid Earth, 123(5), 4041-4062.

https://doi.org/10.5194/egusphere-2026-3037
Preprint. Discussion started: 18 June 2026

Martínez-Garzón, P., Durand, V., Bentz, S., Kwiatek, G., Dresen, G., Turkmen, T., ... & Bohnhoff, M. (2021). Near-fault monitoring reveals combined seismic and slow activation of a fault branch within the Istanbul–Marmara seismic gap in northwest Turkey. Seismological Society of America, 92(6), 3743-3756.

Martinod, J., Hatzfeld, D., Brun, J. P., Davy, P., & Gautier, P. (2000). Continental collision, gravity spreading, and kinematics of Aegea and Anatolia. Tectonics, 19(2), 290-299.

Mason, J., Reicherter, K., & Papanikolaou, I. (2015). The Lapithas Mountain faults and nearby archaeological damage, western Peloponnese, Greece. Z. Geomorphol. Suppl. Issues, 59(4), 189-213.

Mcclusky, S., Balassanian, S., Barka, A., Demir, C., Ergintav, S., Georgiev, I., ... & Veis, G. (2000). Global Positioning System constraints on plate kinematics and dynamics in the eastern Mediterranean and Caucasus. *Journal of Geophysical Research: Solid Earth*, *105*(B3), 5695-5719.

Melis, N., Tselentis, G., & Sokos, E. (1994). The pyrgos (March 26, 1993; Ms= 5.2) earthquake sequence as it was recordrd by the Patras seismic network. Δελτίον της Ελληνικής Γεωλογικής Εταιρίας, 30(5), 175-180.

Michelini, A., Cianetti, S., Gaviano, S., Giunchi, C., Jozinović, D., & Lauciani, V. (2021). INSTANCE–the Italian seismic dataset for machine learning. Earth System Science Data, 13(12), 5509-5544.

Miller, S. A. (2020). Aftershocks are fluid-driven and decay rates controlled by permeability dynamics. Nature communications, 11(1), 5787.

Münchmeyer, J. (2024). PyOcto: A high-throughput seismic phase associator. Seismica, 3(1). https://doi.org/10.26443/seismica.v3i1.1130

National Observatory of Athens, Institute of Geodynamics, Athens. (1975). National Observatory of Athens Seismic Network [Data set]. International Federation of Digital Seismograph Networks. https://doi.org/10.7914/SN/HL

Pacchiani, F., & Lyon-Caen, H. (2010). Geometry and spatio-temporal evolution of the 2001 Agios Ioanis earthquake swarm (Corinth Rift, Greece). Geophysical Journal International, 180(1), 59-72.

Papadopoulos, G. A., Karastathis, V., Kontoes, C., Charalampakis, M., Fokaefs, A., & Papoutsis, I. (2010). Crustal deformation associated with east Mediterranean strike–slip earthquakes: The 8 June 2008 Movri (NW Peloponnese), Greece, earthquake (Mw6. 4). Tectonophysics, 492(1-4), 201-212.

Papanikolaou, D., Fountoulis, I., & Metaxas, C. (2007). Active faults, deformation rates and Quaternary paleogeography at Kyparissiakos Gulf (SW Greece) deduced from onshore and offshore data. Quaternary International, 171, 14-30.

Papazachos, B.C., Papadimitriou, E.E., Kiratzi, A.A., Papazachos, C.B., Louvari, E.K. (1998). Fault plane solutions in the Aegean Sea and the surrounding area and their tectonic implication. Boll. Geofis. Teor. Appl. 39, 199 – 218.

Pérouse, E., Sébrier, M., Braucher, R., Chamot-Rooke, N., Bourlès, D., Briole, P., ... & Arsenikos, S. (2017). Transition from collision to subduction in Western Greece: the Katouna–Stamna active fault system and regional kinematics. International Journal of Earth Sciences, 106(3), 967-989.

Pondrelli, S. (2002). European-Mediterranean Regional Centroid-Moment Tensors Catalog (RCMT) [Data set]. Istituto Nazionale di Geofisica e Vulcanologia (INGV). https://doi.org/10.13127/rcmt/euromed

https://doi.org/10.5194/egusphere-2026-3037
Preprint. Discussion started: 18 June 2026

Pondrelli, S., Salimbeni, S., Ekström, G., Morelli, A., Gasperini, P., & Vannucci, G. (2006). The Italian CMT dataset from 1977 to the present. Physics of the Earth and Planetary Interiors, 159(3-4), 286-303.

Prieto, G. A. (2022). The multitaper spectrum analysis package in Python. Seismological Society of America, 93(3), 1922-1929.

Reilinger, R., McClusky, S., Vernant, P., Lawrence, S., Ergintav, S., Cakmak, R., ... & Karam, G. (2006). GPS constraints on continental deformation in the Africa-Arabia-Eurasia continental collision zone and implications for the dynamics of plate interactions. Journal of Geophysical Research: Solid Earth, 111(B5).

Reverso, T., Marsan, D., & Helmstetter, A. (2015). Detection and characterization of transient forcing episodes affecting earthquake activity in the Aleutian Arc system. Earth and Planetary Science Letters, 412, 25-34.

Ross, Z. E., Ben-Zion, Y., White, M. C., & Vernon, F. L. (2016). Analysis of earthquake body wave spectra for potency and magnitude values: Implications for magnitude scaling relations. Geophysical Supplements to the Monthly Notices of the Royal Astronomical Society, 207(2), 1158-1164.

Ross, Z. E., Rollins, C., Cochran, E. S., Hauksson, E., Avouac, J. P., & Ben-Zion, Y. (2017). Aftershocks driven by afterslip and fluid pressure sweeping through a fault-fracture mesh. *Geophysical Research Letters*, *44*(16), 8260-8267.

Ross, Z. E., Cochran, E. S., Trugman, D. T., & Smith, J. D. (2020). 3D fault architecture controls the dynamism of earthquake swarms. Science, 368(6497), 1357-1361.

Sachpazi, M., Kapetanidis, V., Charalampakis, M., Laigle, M., Kissling, E., Fokaefs, A., ... & Hirn, A. (2020). Methoni Mw 6.8 rupture and aftershocks distribution from a dense array of OBS and land seismometers, offshore SW Hellenic subduction. Tectonophysics, 796, 228643.

Scholz, C. H. (2019). The mechanics of earthquakes and faulting. Cambridge university press.

Shapiro, S. A., Huenges, E., & Borm, G. (1997). Estimating the crust permeability from fluid-injection-induced seismic emission at the KTB site. Geophysical Journal International, 131(2), F15-F18.

Scordilis, E. M., Kementzetzidou, D., & Papazachos, B. C. (2016). Local magnitude calibration of the Hellenic unified seismic network. Journal of Seismology, 20, 319-332.

Serpetsidaki, A., Sokos, E., Tselentis, G. A., & Zahradník, J. (2010). Seismic sequence near Zakynthos Island, Greece, April 2006: Identification of the activated fault plane. Tectonophysics, 480(1-4), 23-32.

Serpetsidaki, A., Elias, P., Ilieva, M., Bernard, P., Briole, P., Deschamps, A., ... & Tselentis, G. A. (2014). New constraints from seismology and geodesy on the M w= 6.4 2008 Movri (Greece) earthquake: evidence for a growing strike-slip fault system. Geophysical Journal International, 198(3), 1373-1386.

Shipton, Z. K., Evans, J. P., Kirschner, D., Kolesar, P. T., Williams, A. P., & Heath, J. (2004). Analysis of CO2 leakage through 'low-permeability'faults from natural reservoirs in the Colorado Plateau, east-central Utah.

Sokos, E. N., & Zahradník,, J. (2008). ISOLA a Fortran code and a Matlab GUI to perform multiple-point source inversion of seismic data. Computers & Geosciences, 34(8), 967-977.

https://doi.org/10.5194/egusphere-2026-3037
Preprint. Discussion started: 18 June 2026

Sokos, E., & Zahradník, J. (2013). Evaluating centroid-moment-tensor uncertainty in the new version of ISOLA software. Seismological Research Letters, 84(4), 656-665.

Uhrhammer, R. A., & Collins, E. R. (1990). Synthesis of Wood-Anderson seismograms from broadband digital records. Bulletin of the Seismological Society of America, 80(3), 702-716.

Uieda, L., Tian, D., Leong, W. J., Jones, M., Schlitzer, W., Toney, L., ... & Wessel, P. (2021). PyGMT: A Python interface for the generic mapping tools. *Zenodo*.

University of Athens. (2008). Hellenic Seismological Network, University of Athens, Seismological Laboratory [Data set]. International Federation of Digital Seismograph Networks. https://doi.org/10.7914/SN/HA

University of Patras. (2000). University of Patras, Seismological Laboratory [Data set]. International Federation of Digital Seismograph Networks. https://doi.org/10.7914/SN/HP

Utsu, T., & Ogata, Y. (1995). The centenary of the Omori formula for a decay law of aftershock activity. Journal of Physics of the Earth, 43(1), 1-33.

Utsu, T. (2002). Statistical features of seismicity. In International geophysics (Vol. 81, pp. 719-732). Academic Press.

van der Elst, N. J. (2021). B-positive: A robust estimator of aftershock magnitude distribution in transiently incomplete catalogs. Journal of Geophysical Research: Solid Earth, 126(2), e2020JB021027.

Wessel, P., Luis, J. F., Uieda, L. A., Scharroo, R., Wobbe, F., Smith, W. H., & Tian, D. (2019). The generic mapping tools version 6. *Geochemistry, Geophysics, Geosystems*, *20*(11), 5556-5564.

Wiemer, S., & Wyss, M. (2000). Minimum magnitude of completeness in earthquake catalogs: Examples from Alaska, the western United States, and Japan. Bulletin of the seismological society of America, 90(4), 859-869.

Woessner, J., & Wiemer, S. (2005). Assessing the quality of earthquake catalogues: Estimating the magnitude of completeness and its uncertainty. Bulletin of the Seismological Society of America, 95(2), 684-698.

Woollam, J., Münchmeyer, J., Tilmann, F., Rietbrock, A., Lange, D., Bornstein, T., ... & Soto, H. (2022). SeisBench—A toolbox for machine learning in seismology. Seismological Society of America, 93(3), 1695-1709.

Zahradník, J., & Sokos, E. (2018). ISOLA code for multiple-point source modeling. In Moment tensor solutions: A useful tool for seismotectonics (pp. 1-28). Cham: Springer International Publishing.

Zaliapin, I., & Ben-Zion, Y. (2013a). Earthquake clusters in southern California I: Identification and stability. Journal of Geophysical Research: Solid Earth, 118(6), 2847-2864.

Zaliapin, I., & Ben-Zion, Y. (2013b). Earthquake clusters in southern California II: Classification and relation to physical properties of the crust. Journal of Geophysical Research: Solid Earth, 118(6), 2865-2877.

Zaliapin, I., & Ben-Zion, Y. (2020). Earthquake declustering using the nearest-neighbor approach in space-time-magnitude domain. Journal of Geophysical Research: Solid Earth, 125(4), e2018JB017120.

Zhu, W., & Beroza, G. C. (2019). PhaseNet: a deep-neural-network-based seismic arrival-time picking method. Geophysical Journal International, 216(1), 261-273.